

Retention and permeability properties of damaged porous rocks

Jean-Michel Pereira, Chloé Arson

► **To cite this version:**

Jean-Michel Pereira, Chloé Arson. Retention and permeability properties of damaged porous rocks. Computers and Geotechnics, Elsevier, 2013, 48, pp.272-282. 10.1016/j.compgeo.2012.08.003 . hal-00800887

HAL Id: hal-00800887

<https://hal-enpc.archives-ouvertes.fr/hal-00800887>

Submitted on 2 May 2019

HAL is a multi-disciplinary open access archive for the deposit and dissemination of scientific research documents, whether they are published or not. The documents may come from teaching and research institutions in France or abroad, or from public or private research centers.

L'archive ouverte pluridisciplinaire **HAL**, est destinée au dépôt et à la diffusion de documents scientifiques de niveau recherche, publiés ou non, émanant des établissements d'enseignement et de recherche français ou étrangers, des laboratoires publics ou privés.

Retention and Permeability Properties of Damaged Porous Rocks

Jean-Michel PEREIRA^{a,*}, Chloé ARSON^b

^a*Université Paris-Est, Laboratoire Navier (UMR CNRS – IFSTTAR – ENPC),
CERMES, École des Ponts ParisTech, France*

^b*Zachry Department of Civil Engineering, Texas A&M University, USA*

Abstract

The objective of this research work is to model the influence of deformation and damage on the permeability and retention properties of cracked porous media. This is achieved thanks to the introduction of microscale information into a macroscopic damage model. To this end, the Pore Size Distribution (PSD) of the material is coupled to the mechanical behaviour of the rock. Changes to this distribution due to deformation and damage are modelled and then used to capture induced changes to the retention and permeability properties of partially saturated materials.

Rock microstructure is characterized by the Size Distributions of natural pores and cracks, which are used to update intrinsic permeability with Hagen-Poiseuille flow equation and Darcy's law. The void space occupied by water is computed by integrating the Pore Size Distributions of natural pores and cracks up to the capillary pore radius (r_{sat}). Laplace equation is used to relate r_{sat} to the capillary pressure.

*École des Ponts ParisTech, 6-8 av. B. Pascal, F-77455 Marne-la-Vallée cedex 2, FRANCE. email: jeanmichel.pereira@enpc.fr

The paper explains how to update PSD parameters with the macroscopic variables (such as deformation and damage), and then how to update permeability and retention properties with the PSD parameters. Conventional triaxial compression tests are simulated under controlled capillary pressure and under controlled water content. The proposed model captures well the intrinsic permeability decrease associated to the elastic compression of the natural pores, followed by the permeability jump due to crack opening. The modeling framework can be adapted to any rock constitutive model, including thermo-hydro-chemo-mechanical couplings. Applications may be found in energy production, ore exploitation and waste management.

Keywords: Rock, Poromechanics, Continuum Damage Mechanics, Pore Size Distribution Curve, Permeability, Retention Curve, Numerical Model, Triaxial Compression Test

1. Introduction

Multiphase flow in damaged porous media became a key topic in research related to oil and gas extraction [1, 2]. The urge to find new mineral deposits has also generated a lot of research on the influence of crystallization and dissolution processes occurring in the deep Earth crust on porosity and permeability of rock [3, 4]. Relating rock microstructure to porosity, permeability and retention properties is of prior importance in problems involving pore fluid phase changes, such as the design of deep nuclear waste disposals [5, 6] and geothermal boreholes [7, 8].

The first models based on the knowledge of the Pore Size Distribution (PSD) curve focused on unimodal porous media [9, 10]. More recent studies use the

12 PSD curve to determine the retention and permeability properties of bimodal
13 porous media [11, 12, 13, 14]. However, these studies deal with undamaged
14 materials. Following a micromechanical approach, Zhou et al. [15] intro-
15 duced a penetration distance to account for crack connectivity. However,
16 permeability is computed from a PSD curve that needs to be integrated in
17 each possible micro-crack direction, which induces high computational costs.
18 In dual permeability models proposed for fracture networks, flow in natural
19 pores and cracks are governed by different equations, that may be coupled
20 or not [16, 17, 18, 19]. In multimodal models [20], natural pores and cracks
21 are assumed to connect and to form a unique porous network, which avoids
22 the computation of coefficients accounting for the transfer of fluid from one
23 network to the other. Statistical methods make it possible to account for
24 the crack locations, lengths, apertures and orientations [21]. The main chal-
25 lenges in fracture network models are: the determination of equivalent flow
26 properties at the scale of the Representative Elementary Volume [22, 23], the
27 computation of internal length parameters, and the prediction of percolation
28 thresholds. Moreover, most of the fracture network models do not account
29 for the deformation of the solid skeleton nor the evolution of damage. Double
30 porosity models overcome this limitation: for instance, Wong et al. [24] pro-
31 posed to equate fluid flow from one porous network to the other as a phase
32 change.

33 A few phenomenological models based on Continuum Damage Mechanics
34 account for the effect of cracking on permeability changes. It is usually as-
35 sumed that crack permeability adds to the permeability of the undamaged
36 rock matrix [25]. In anisotropic models, the flow induced by damage is often

37 considered to occur in the crack planes, which makes it possible to compute
38 crack permeability from the cubic law [26, 27]. Maleki and Pouya [28, 29]
39 proposed a more refined approach relying on empirical percolation thresh-
40 olds.

41 The objective of this research work is to extend the model presented in [30]
42 to unsaturated porous rock, in order to assess the influence of deformation
43 and damage on the permeability and retention properties of cracked porous
44 media. The proposed approach consists in updating Pore Size Distributions
45 (PSD) with macroscopic variables of deformation and damage. Section 2
46 explains how PSD parameters are related to the volume occupied by natural
47 pores and cracks, and how to update these volume fractions with deforma-
48 tion and damage. Section 3 details the permeability and retention models,
49 and presents the method to compute the intrinsic permeability, the degree
50 of saturation and the relative permeability. Conventional triaxial compres-
51 sion tests have been simulated. The results obtained for tests controlled in
52 capillary pressure are presented in Section 4, and the simulations performed
53 at fixed water content are presented in Section 5.

54 **2. Representation of the Damaged Microstructure**

55 *2.1. Background: Crack-Induced Porosity and Permeability in Rock*

56 Cracks are naturally present in most rock materials [31, 32]. As a result,
57 measuring damage requires the definition of a reference state, in which rock
58 connected porosity is associated to a “natural” void space. In this paper, nat-
59 ural porosity is defined as the porosity measured before loading the sample.
60 In the simulations presented in the sequel, the material of interest is granite

61 rock. Unweathered granite subjected to low pressure and low temperature
62 gradients has a natural porosity, due to micro-cracks with a length lower
63 than the micron. Weathered granite shows a bimodal porosity [33]: drying
64 processes favor the penetration and crystallization of salt in the rock, which
65 creates new void space in the range of sizes of natural pores as well as one
66 order of magnitude higher than natural pores (Fig. 1). This gap in the pore
67 size distribution has also been observed in clay rock damaged by mechanical
68 stress: the typical crack length is one to two orders of magnitude larger than
69 the average natural pore radius [28]. The main geomechanical applications
70 of the proposed permeability model are expected to be found in excavation
71 and geological storage problems, which involve high pressure gradients (of
72 the order of 10 MPa or higher). According to the observations reported in
73 the literature, the permeability model proposed in the sequel assumes that
74 natural pores and cracks form two separate sets of pores. Each set of pores is
75 characterized by a Pore Size Distribution (PSD). In addition, natural poros-
76 ity induces some permeability, even if the latter is low (of the order of 10^{-15}
77 m^2 in granite, for instance). Because cracks are typically one to two orders
78 of magnitude larger (or longer) than natural pores, it is expected that cracks
79 will intersect the connected natural porous network, even in the absence of
80 crack coalescence. As a result, it is assumed that: (1) natural pores and
81 cracks will form a unique, bimodal connected porous network, and (2) any
82 occurrence of damage will enhance permeability. These two assumptions are
83 justified by recent permeability measurements obtained by wave propagation
84 techniques [34] (Fig. 1). However, the present model is restricted to non-
85 interacting cracks, which explains the absence of percolation threshold in the

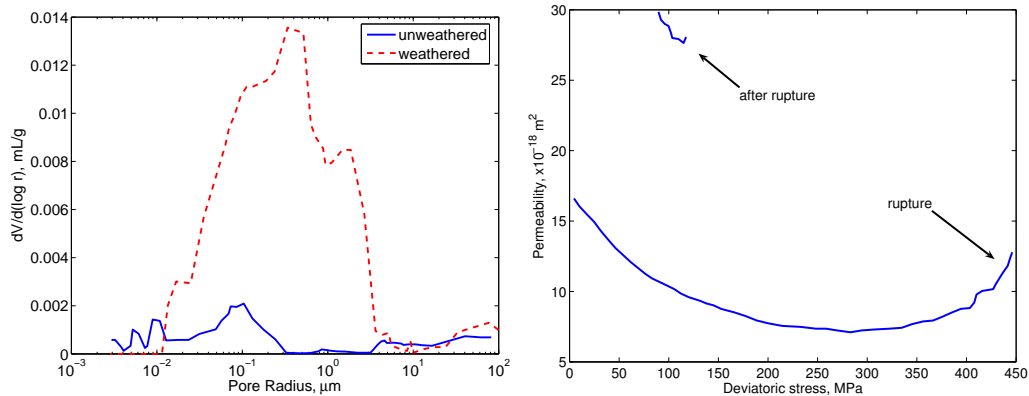


Figure 1: Damage effects on microstructure and permeability of rocks. (a) Influence of weathering damage on granite microstructure (left, modified from [33]): unimodal porosity of unweathered granite versus bimodal porosity of weathered granite. (b) Influence of damage on intrinsic permeability in saturated basalt during a triaxial compression test (right, modified from [34]).

86 formulation. The permeability-porosity model is based on a micro-macro
 87 coupling between natural and damage-induced porosities on the one hand,
 88 and deformation and damage variables on the other hand. The permeability
 89 model presented in this paper aims to:

- 90 1. capture crack-induced intrinsic permeability enhancement in unsatu-
 91 rated conditions (under control of suction and under control of water
 92 content), as it was observed in saturated conditions [34] (Fig. 1),
- 93 2. predict the trends of the evolution of the water retention curve and of
 94 the relative permeability with damage.

95 2.2. Relationship between Permeability and Porosity

96 It is assumed that natural pores and cracks do not overlap and form a
 97 unique, bimodal porous network. Natural pores and cracks in rock are actu-

98 ally difficult to discriminate, even with the most advanced X-ray tomography
 99 techniques available to date [35, 36, 37, 38]. As explained earlier, some sim-
 100 plifying assumptions are made on rock microstructure in order to permit
 101 simple modelling tools to be developed. Separate sets of pores and cracks
 102 are defined so that it is possible to assign separated Pore Size Distributions
 103 (PSD) to each set. This is a convenient hypothesis that will allow relating
 104 pore volume change to elastic deformation and crack development to damage.
 105 In the present model, the PSD curve of the damaged rock is thus considered
 106 to be the superposition of the PSD curve associated to the natural pores with
 107 the PSD curve associated to the cracks. Following the classical assumption
 108 used to interpret Mercury Intrusion Porosimetry data to experimentally de-
 109 termine PSD curves, the pores are considered as a bundle of parallel cylinders
 110 with various radii. For a unit Representative Elementary Volume (REV), the
 111 “pore size” distribution thus reduces to a “radius size” distribution. Consid-
 112 ering that there are N_p natural pores and N_c cracks in the REV, and noting
 113 $p_p(r)$ (respectively $p_c(r)$) the probability density function of natural pores of
 114 radius r (respectively of cracks of radius r), the number of natural pores of
 115 radius r is equal to $\alpha_p(r) = N_p p_p(r)$, and the number of cracks of radius r
 116 is equal to $\alpha_c(r) = N_c p_c(r)$. For a unit REV, the pores “volume frequency”
 117 is equal to the pores “area frequency” [9]: $\alpha_p(r)\pi r^2$ for natural pores, and
 118 $\alpha_c(r)\pi r^2$ for cracks. As a result, the volume occupied by the pores in the
 119 REV can be defined as:

$$V_k = \int_{r_{min}^k}^{r_{max}^k} \alpha_k(r)\pi r^2 dr = \pi N_k \int_{r_{min}^k}^{r_{max}^k} p_k(r)r^2 dr, \quad k = p, c \quad (1)$$

120 where r_{min}^k and r_{max}^k are the minimum and maximum pore radius values
 121 ($k = p$ for natural pores, $k = c$ for cracks). It is assumed that natural

122 pores and cracks do not overlap, but are connected. This assumption is
 123 similar to a common thought model used in homogenization theories [39], in
 124 which pores are viewed as pore spaces connected to each other by fictitious
 125 “channels” of zero volume. As a result, total porosity is the sum of pore and
 126 crack porosities, but total intrinsic permeability is not the sum of pore and
 127 crack permeabilities. Assuming that the flow in the virtual bundle of parallel
 128 cylinders is laminar, the intrinsic permeability of the damaged rock can be
 129 computed by combining Hagen-Poiseuille flow equation to Darcy’s law [9]:

$$k_{int} = \frac{\Phi}{8 \int_0^\infty f(r) dr} \int_0^\infty f(r) r^2 dr \quad (2)$$

130 in which Φ is the total porosity of the medium (accounting for natural pores
 131 and cracks). Assuming that all pore cuts are circles actually implies that the
 132 direction of the flow is assumed to be parallel to the direction of the pores
 133 [40]. Recalling that natural pores and cracks are assumed to connect without
 134 overlapping, and that the length of the REV in the direction of the flow is
 135 assumed to be equal to unity, the “volume frequency” $f(r)$ is equal to the
 136 “area frequency”:

$$\begin{aligned} f(r) = & H(r - r_{min}^p) H(r_{max}^p - r) N_p p_p(r) \pi r^2 \\ & + H(r - r_{min}^c) H(r_{max}^c - r) N_c p_c(r) \pi r^2 \end{aligned} \quad (3)$$

137 in which H is Heaviside function.

138 *2.3. Relationship between Porosity and Macroscopic Variables*

139 The macroscopic damage variable is defined as the spectral decomposition
 140 of the second-order crack density tensor [41, 42]:

$$\Omega = \sum_{k=1}^3 d_k \mathbf{n}^k \otimes \mathbf{n}^k \quad (4)$$

141 Total deformation is the sum of a damage-induced deformation $\boldsymbol{\epsilon}^d$ and a
 142 purely elastic deformation $\boldsymbol{\epsilon}^{el}$ (i.e. the deformation that would be obtained
 143 if the stiffness tensor were undamaged):

$$\boldsymbol{\epsilon} = \boldsymbol{\epsilon}^{el} + \boldsymbol{\epsilon}^d = \boldsymbol{\epsilon}^{el} + \boldsymbol{\epsilon}^{ed} + \boldsymbol{\epsilon}^{id} \quad (5)$$

144 $\boldsymbol{\epsilon}^{ed}$ is the additional elastic deformation induced by the degradation of stiff-
 145 ness with cracking. Due to the existence of residual crack opening after
 146 unloading, damage not only reduces the material rigidity, but also induces
 147 irreversible strains ($\boldsymbol{\epsilon}^{id}$) [43]. At a given state of damage, the volume occu-
 148 pied by the non-interactig cracks is defined as:

$$V_c = -Tr(\boldsymbol{\epsilon}^{ed} + \boldsymbol{\epsilon}^{id}) = -Tr(\boldsymbol{\epsilon}^d) \quad (6)$$

149 in which the soil mechanics sign convention is used (compression counted
 150 positive). The volume occupied by natural pores is assumed to evolve with
 151 the purely elastic deformation:

$$V_p = -Tr(\boldsymbol{\epsilon}^{el}) \quad (7)$$

152 The knowledge of the volume occupied by the natural pores and cracks (ex-
 153 pressed in equation 1) makes it possible to update porosity and the “area
 154 frequency” defined in equation 3, and thus, to update the intrinsic perme-
 155 ability (expressed in equation 2). Natural pores and cracks volumes can

156 be calculated at any loading step (with equations 6 and 7), as long as a
 157 constitutive model is provided to relate stress to damage and deformation.
 158 To illustrate the proposed conceptual framework, a simple mechanical dam-
 159 age model has been adopted in the simulations presented in the sequel: it
 160 is assumed that damage grows with tensile strains according to a common
 161 damage criterion [44, 45]:

$$f_d(\boldsymbol{\Omega}, \boldsymbol{\epsilon}^+) = \sqrt{\frac{1}{2}(g\boldsymbol{\epsilon}^+) : (g\boldsymbol{\epsilon}^+) - C_0 - C_1 \boldsymbol{\delta} : \boldsymbol{\Omega}} \quad (8)$$

162 in which $\boldsymbol{\delta}$ is the second-order identity tensor. The parameter g relates the
 163 damage tensor to the compression stress ($\boldsymbol{\sigma}^R$) that would be necessary to
 164 close the residual cracks formed after a tensile loading followed by a bare
 165 unloading [46]: $\boldsymbol{\sigma}^R = -g\boldsymbol{\Omega}$. C_0 is the initial damage threshold, and C_1
 166 controls cracks growth with cumulated damage. The damage flow rule is
 167 assumed to be associated.

168 2.4. Updating Porous Volume Fractions with Macroscopic Variables

169 For a strain-controlled test, the increment of strain applied at iteration k
 170 is known. A trial increment of stress is computed, assuming that the material
 171 remains elastic during the loading iteration:

$$d\boldsymbol{\sigma}^{(k,*)} = \mathbf{D}(\boldsymbol{\Omega}^{(k-1)}) : d\boldsymbol{\epsilon}^{(k)} \quad (9)$$

172 In the mechanical damage model selected as an illustration of the conceptual
 173 framework, the damaged elasticity tensor $\mathbf{D}(\boldsymbol{\Omega})$ is computed by applying
 174 the Principle of Equivalent Elastic Energy (PEEE):

$$\mathbf{D}(\boldsymbol{\Omega}) = \mathbf{M}^{-1}(\boldsymbol{\Omega}) : \mathbf{D}_0 : \mathbf{M}^{-T}(\boldsymbol{\Omega}) \quad (10)$$

175 in which $\mathbf{M}(\boldsymbol{\Omega})$ is the fourth-order damage operator introduced by Cordebois
 176 and Sidoroff to define effective stress $\tilde{\boldsymbol{\sigma}}$ [47]:

$$\tilde{\boldsymbol{\sigma}} = \mathbf{M}(\boldsymbol{\Omega}) : \boldsymbol{\sigma} = (\boldsymbol{\delta} - \boldsymbol{\Omega})^{-1/2} : \boldsymbol{\sigma} : (\boldsymbol{\delta} - \boldsymbol{\Omega})^{1/2} \quad (11)$$

177 in which $\boldsymbol{\delta}$ denotes the second-order identity tensor. If the undamaged mate-
 178 rial is linear elastic, with a Young's modulus E_0 and a Poisson's ratio ν_0 , the
 179 damaged stiffness tensor obtained by combining Equations 10 and 11 writes,
 180 using Voigt notations [48]:

$$\mathbf{D}(\boldsymbol{\Omega}) = \frac{E_0}{(1-2\nu_0)(1+\nu_0)} \times \left[\begin{array}{ccc} (1-\nu_0)(1-d_1)^2 & \nu_0(1-d_1)(1-d_2) & \nu_0(1-d_1)(1-d_3) \\ \nu_0(1-d_1)(1-d_2) & (1-\nu_0)(1-d_2)^2 & \nu_0(1-d_2)(1-d_3) \\ \nu_0(1-d_1)(1-d_3) & \nu_0(1-d_2)(1-d_3) & (1-\nu_0)(1-d_3)^2 \\ 0 & 0 & 0 \\ 0 & 0 & 0 \\ 0 & 0 & 0 \\ 0 & 0 & 0 \\ 0 & 0 & 0 \\ (1-2\nu_0)(1-d_2)(1-d_3) & 0 & 0 \\ 0 & (1-2\nu_0)(1-d_1)(1-d_3) & 0 \\ 0 & 0 & (1-2\nu_0)(1-d_1)(1-d_2) \end{array} \right] \quad (12)$$

181 in which the d_k refer to damage eigenvalues (Eq. 4). Total strains are updated
 182 with the known incremental strains:

$$\boldsymbol{\epsilon}^{(k)} = \boldsymbol{\epsilon}^{(k-1)} + d\boldsymbol{\epsilon}^{(k)} \quad (13)$$

183 The sign of the damage criterion (Equation 8) is checked. If damage occurs
 184 during the iteration, the stress increment is updated as follows:

$$d\boldsymbol{\sigma} = \mathbf{D}(\boldsymbol{\Omega}) : d\boldsymbol{\epsilon} + \left(\frac{\partial \mathbf{D}(\boldsymbol{\Omega})}{\partial \boldsymbol{\Omega}} : \boldsymbol{\epsilon} \right) : d\boldsymbol{\Omega} - d(\mathbf{D}(\boldsymbol{\Omega}) : \boldsymbol{\epsilon}^{id}) \quad (14)$$

185 By definition of the damage-induced residual stress and residual strains
 186 ($\boldsymbol{\sigma}^R = -g\boldsymbol{\Omega} = \mathbf{D}(\boldsymbol{\Omega}) : \boldsymbol{\epsilon}^{id}$):

$$d\boldsymbol{\sigma} = \mathbf{D}(\boldsymbol{\Omega}) : d\boldsymbol{\epsilon} + \left(\frac{\partial \mathbf{D}(\boldsymbol{\Omega})}{\partial \boldsymbol{\Omega}} : \boldsymbol{\epsilon} \right) : d\boldsymbol{\Omega} + gd\boldsymbol{\Omega} \quad (15)$$

187 If damage occurs at iteration k , the stress increment is updated with the
 188 imposed strain increment as follows:

$$d\boldsymbol{\sigma}^{(k)} = \mathbf{D}(\boldsymbol{\Omega}^{(k-1)}) : d\boldsymbol{\epsilon}^{(k)} + \left(\frac{\partial \mathbf{D}(\boldsymbol{\Omega}^{(k-1)})}{\partial \boldsymbol{\Omega}} : \boldsymbol{\epsilon}^{(k-1)} \right) : d\boldsymbol{\Omega}^{(k)} + gd\boldsymbol{\Omega}^{(k)} \quad (16)$$

189 After updating total strains, it is possible to get the volume of pores ($V_v =$
 190 $V_p + V_c$) in the REV at iteration k :

$$\boldsymbol{\epsilon}^{(k)} = \boldsymbol{\epsilon}^{(k-1)} + d\boldsymbol{\epsilon}^{(k)}, \quad V_v^{(k)} = -Tr(\boldsymbol{\epsilon}^{(k)}) + \Phi_0 \quad (17)$$

191 in which Φ_0 is the initial porosity of the rock (assumed to be initially un-
 192 damaged). For any iteration, in loading or unloading conditions:

$$d\boldsymbol{\epsilon}^{el(k)} = \mathbf{D}(\boldsymbol{\Omega}^{(k-1)})^{-1} : d\boldsymbol{\sigma}^{(k)} \quad (18)$$

193 The combination of Equations 17 and 18 gives:

$$d\boldsymbol{\epsilon}^{d(k)} = d\boldsymbol{\epsilon}^{(k)} - d\boldsymbol{\epsilon}^{el(k)}, \quad \boldsymbol{\epsilon}^{d(k)} = \boldsymbol{\epsilon}^{d(k-1)} + d\boldsymbol{\epsilon}^{d(k)} \quad (19)$$

194 from which it is possible to update the volume fractions of cracks and natural
 195 pores (Equations 6 and 7):

$$V_c^{(k)} = -Tr \left(\epsilon^{d(k)} \right), \quad V_p^{(k)} = V_v^{(k)} - V_c^{(k)} \quad (20)$$

196 3. Computation of Permeability and Degree of Saturation

197 3.1. Constitutive Model

198 When the porous network is filled with two fluids, the non-wetting fluid
 199 is defined as the one that has a contact angle (θ_{nw}) greater than 90° , and the
 200 wetting fluid is defined as the fluid that has a contact angle (θ_w) less than
 201 90° . Capillary pressure (p_c) is defined as the difference between the pressure
 202 of the non-wetting fluid (p_{nw}) and the pressure of the wetting fluid (p_w),
 203 and is related to the capillary pore radius (r_{sat}) by the Washburn-Laplace
 204 equation [9, 11]:

$$p_c = p_{nw} - p_w = \frac{2\sigma_{nw/w} \cos \theta_w}{r_{sat}} \quad (21)$$

205 in which $\sigma_{nw/w}$ is the surface tension in the meniscus separating the two fluid
 206 phases. In many approaches [9, 11], it is assumed that the tubes constituting
 207 the porous network are either saturated with the wetting fluid, or completely
 208 filled with the non-wetting fluid. With this assumption, equation 21 may be
 209 interpreted as follows:

- 210 • for $r > r_{sat}$, $p_c(r) < p_c$, i.e. the capillary pressure p_c is higher than
 211 the capillary pressure ensuring the equilibrium of the meniscus, so the
 212 tube is filled with the non-wetting fluid,

213 • for $r < r_{sat}$, $p_c(r) > p_c$, i.e. the capillary pressure p_c is lower than the
214 capillary pressure ensuring the equilibrium of the meniscus, so the tube
215 is filled with the wetting fluid.

216 In the present approach, according to the postulate of local state, any evo-
217 lution is considered as the succession of incremental evolutions between two
218 equilibrium states. This amounts to say that transient effects associated to
219 drying/wetting processes are neglected. To model the time history of the sat-
220 uration process, a more refined representation of the microstructure would be
221 needed. Blunt et al. studied the evolution of the capillary fringe by making
222 a distinction between pores and throats [49, 50]. In order to account for the
223 presence of residual films of the wetting phase during draining paths, Blunt
224 proposed to model the porous space as a network of cylinders of triangular
225 section [51]. Wettability variations can be accounted for due to the presence
226 of corners in the shape of the pores cross section. In its current development,
227 the proposed model assumes that pores are circular cylinders, and saturation
228 history is not accounted for. If the current capillary pressure is known, it is
229 thus possible to determine the value of the pore radius satisfying equation
230 21 (noted r_{sat}). Without loosing the general validity of the presented frame-
231 work, the wetting fluid is assumed to be liquid water, and the non-wetting
232 fluid is assumed to be gaseous air. The volume of water in the REV (V_w)
233 is equal to the volume of the pores that have a radius lower than r_{sat} . As
234 a result, V_w is obtained by restricting the integral of the volume frequencies
235 (equation 1) to the appropriate interval. At this point, it is essential to figure
236 out in which family of pores (either natural or cracks) r_{sat} is located. Since it
237 is assumed that these families do not overlap (i.e. $r_{max}^p < r_{min}^c$), V_w is simply

238 obtained by:

$$V_w = \int_{r_{min}^p}^{r_{sat}} H(r_{sat} - r_{min}^p) H(r_{max}^p - r_{sat}) \alpha_p(r) \pi r^2 dr \quad (22)$$

239 if $r_{sat} \in [r_{min}^p, r_{max}^p]$ and by:

$$V_w = V_p + \int_{r_{min}^c}^{r_{sat}} H(r_{sat} - r_{min}^c) H(r_{max}^c - r_{sat}) \alpha_c(r) \pi r^2 dr \quad (23)$$

240 if $r_{sat} \in [r_{min}^c, r_{max}^c]$. The degree of saturation is defined as:

$$S_w = \frac{V_w}{V_p + V_c} \quad (24)$$

241 Noting V_{REV} the Representative Elementary Volume, we have: $V_v = \int_0^\infty f(r) dr$

242 and $\Phi = V_v/V_{REV}$. As a result, combining equations 1, 2 and 3 provides the

243 expression of the damaged intrinsic rock permeability:

$$k_{int} = \frac{1}{8 V_{REV}} \left(\int_{r_{min}^p}^{r_{max}^p} \alpha_p(r) \pi r^4 dr + \int_{r_{min}^c}^{r_{max}^c} \alpha_c(r) \pi r^4 dr \right) \quad (25)$$

244 The total (or apparent) permeability of the damaged unsaturated can be

245 expressed in the same way as:

$$k_w = \frac{1}{8 V_{REV}} \int_{r_{min}^p}^{r_{sat}} H(r_{sat} - r_{min}^p) H(r_{max}^p - r_{sat}) \alpha_p(r) \pi r^4 dr \quad (26)$$

246 if $r_{sat} \in [r_{min}^p, r_{max}^p]$ and as:

$$k_w = \frac{1}{8 V_{REV}} \int_{r_{min}^p}^{r_{max}^p} H(r_{sat} - r_{min}^p) H(r_{max}^p - r_{sat}) \alpha_p(r) \pi r^4 dr \quad (27)$$

$$+ \frac{1}{8 V_{REV}} \int_{r_{min}^c}^{r_{sat}} H(r_{sat} - r_{min}^c) H(r_{max}^c - r_{sat}) \alpha_c(r) \pi r^4 dr$$

247 if $r_{sat} \in [r_{min}^c, r_{max}^c]$. The relative permeability k_R can then be obtained using

248 the following relation:

$$k_R = k_w/k_{int} \quad (28)$$

249 *3.2. Computational Algorithm*

250 The computational algorithm to update permeability and retention prop-
251 erties with macroscopic variables is summarized below. Interested readers are
252 referred to [30] for a detailed version of the algorithm related to the damage
253 and its effects on permeability of saturated rocks.

- 254 1. The main steps to update the volume fractions of natural pores and
255 cracks in a strain-controlled test are indicated in Subsection 2.4.
- 256 2. Once V_p and V_c are known, it is possible to update the parameters
257 of the probability functions $p_p(r)$ and $p_c(r)$. In the simulations pre-
258 sented in the sequel, the radius size of natural pores follows a Gauss
259 distribution [10], and the radius size of cracks follows an exponential
260 distribution [28]. Crack length (λ_c) is the only parameter of the expo-
261 nential distribution $p_c(r)$. λ_c is assumed to be a fixed parameter of the
262 model, and is computed by using the mathematical definition of the
263 mean value of a random variable. The number of cracks in the Repre-
264 sentative Elementary Volume (N_c) is then updated with V_c (equation
265 1). Given the initial void ratio, it is also possible to use definitions of
266 the theory of probabilities in order to compute the initial number of
267 natural pores (N_p^0), the initial standard deviation (s^0) and the initial
268 mean value of the natural pores (m^0). After the initial stage, N_p and
269 s are considered fixed parameters of the model and the mean radius of
270 natural pores is updated with V_p (equation 1). In practice, the value
271 of the standard deviation used in the resolution algorithm was fixed to
272 one third of the range of values $[r_p^{min}, r_p^{max}]$. The model parameters
273 were post-processed for various choices of $s = s^0$ to verify that the

274 simulation results presented in the following were not sensitive to the
275 choice of s^0 for the pore sizes considered.

276 3. Once the parameters of the probability density functions have been
277 updated with the macroscopic variables, it is possible to update the
278 intrinsic permeability according to equation 25.

279 4. The final step consists in determining r_{sat} .

280 • If the test is performed with a control of capillary pressure, r_{sat}
281 is computed by using Laplace equation (equation 21). For water,
282 we have [52]: $\sigma_{nw/w} = 72.75 \cdot 10^{-3}$ N/m and $\cos \theta_w = 1$ (assuming
283 a null contact angle between water and solid). The degree of
284 saturation is updated by using equation 22 or 23 and equation 24,
285 and the relative permeability is computed by combining equation
286 25 and equation 26 or 27.

287 • The procedure differs slightly if the test is performed with a control
288 of water content. First recall that water content (w) is defined as
289 the ratio of the mass of water by the mass of solid grains contained
290 in the sample: $w = M_w/M_s$. Noting e the void ratio of the sample,
291 and G_s the specific gravity of the solid phase, we have [53]:

$$e S_w = w G_s \quad (29)$$

292 G_s is a constant, and w is assumed to be fixed. Assuming that
293 the initial porosity is given, the volume occupied by the voids is
294 known at this stage of the computations (equation 17). The solid
295 phase is considered incompressible, so that the volume occupied
296 by the solid grains at the current iteration is equal to the volume

297 occupied by the solid phase in the initial state: $V_s = 1 - \Phi_0$ for
 298 a unit initial REV. It is thus possible to determine the void ratio
 299 and the degree of saturation at the current iteration:

$$e^{(k)} = \frac{V_v^{(k)}}{V_s}, \quad S_w^{(k)} = \frac{w G_s}{e^{(k)}} \quad (30)$$

300 At high pressures, the assumption of incompressible solid grains
 301 may be unrealistic. The proposed modeling framework can easily
 302 be extended to compressible grains by means of Biot coefficients
 303 [54]. The latter do depend on damage, but this dependence actu-
 304 ally exists due to the dependence of Biot's coefficients on the dam-
 305 aged stiffness tensor, the expression of which is already derived
 306 from principles of Continuum Damage Mechanics in the present
 307 modeling framework. Combining relations 30, 24 and 22 or 23
 308 provides an equation that can be solved for r_{sat} . The capillary
 309 pressure can be obtained by Laplace equation (equation 21) in
 310 order to determine the retention curve at any stage of damage.
 311 The relative permeability is updated by using equation 25 and
 312 equation 26 or 27.

313 It has to be noted that among the nine microscopic parameters involved in
 314 the model formulation (r_{min}^p , r_{max}^p , r_{min}^c , r_{max}^c , N_p , N_c , m , s and λ_c):

- 315 1. the average size of the natural pores (m) and the number of cracks
 316 developed in the REV (N_c) are updated with macroscopic variables
 317 (e.g., deformation and damage),
- 318 2. the number of natural pores (N_p), the standard deviation of the natural
 319 pore size distribution (s) and the crack length (λ_c) are deduced from

320 definitions used in the theory of probability,
321 3. only the ranges of values of the natural pores and cracks (r_{min}^p , r_{max}^p ,
322 r_{min}^c and r_{max}^c) are fixed parameters that need to be provided by the
323 user.

324 The minimum and maximum void sizes observed at a certain state of damage
325 (and in the undamaged configuration in particular) do change as deformation
326 and damage evolve: for instance, the longest crack observed at 10% damage
327 is likely to be shorter than the longest crack observed for 50% damage. The
328 bounds indicated as model parameters herein embrace all the possible values
329 that can be taken by the natural pores and cracks, i.e. for all the states of
330 deformation and damage of the rock before failure. It is understated that
331 the values of pore sizes close to the bounds are “improbable events” in the
332 sense of mathematics (i.e., events with a zero probability of occurrence). The
333 parameters controlling the shape of the PSDs (mainly: N_p , N_c , m , s and λ_c)
334 are thus assumed to be sufficient to capture the main pore size changes in-
335 duced by deformation and damage. As a result, the size that separates pores
336 from cracks is considered as a material parameter. The authors reckon that
337 this is an idealized assumption. However, updating the bounds of pore radii
338 ranges of values would require an update of the size of the Representative
339 Elementary Volume, which constitutes an area of research per se [55].

340 **4. Permeability and Retention Properties with Control of Capil-** 341 **lary Pressure**

342 A conventional triaxial compression test is simulated, by increasing ϵ_1 by
343 increments while maintaining a constant confinement (radial stress is con-

Table 1: Main material parameters used to simulate unconfined triaxial compression tests on Vienne Granite.

E_0 (Pa)	ν_0 (-)	g (Pa)	C_0 (Pa)	C_1 (Pa)	e_0 (-)
$8.01e10$	0.28	$-3.3e8$	$1.1e5$	$2.2e6$	0.008
r_{min}^p (μm)	r_{max}^p (μm)	r_{min}^c (μm)	r_{max}^c (μm)		
0.01	1	1	10		

344 stant, equal to 100 MPa). Capillary pressure is fixed throughout the test
 345 (two tests are simulated, the first at a capillary pressure of 100 kPa and
 346 the second at 300 kPa). The material under study is a granite for which
 347 experimental results on drained triaxial compression tests have already been
 348 published [56]. The mechanical damage model presented in Subsection 2.4
 349 has proved to reproduce well the semi-brittle behavior of this granite [57, 58].
 350 The mechanical parameters (E_0 , ν_0 , g , C_0 , C_1) are taken equal to the ones
 351 that are calibrated in [57, 58]. The initial void ratio (e_0) is taken equal to
 352 the void ratio measured on Vienne granite [56], which is the rock studied in
 353 the calibration presented in [57, 58]. The minimum and maximum radii of
 354 the granite natural pores (r_{min}^p and r_{max}^p) are chosen so that the mean of r_p
 355 can be expected to be of the order of $0.1\mu m$, as stated in [33]. The orders
 356 of magnitude for the minimum and maximum radii of the cracks (r_{min}^c and
 357 r_{max}^c) are chosen according to Maleki [28], who also worked on damage in
 358 rock materials. The main material parameters are summarized in Table 1.

359 Figure 2 presents the deviatoric stress and damage variable as functions
360 of the imposed axial strain. The first stage corresponding to the isotropic
361 compression from 0 to 100 MPa is also plotted. As already shown in previous
362 studies, damage occurs when shear strains start to increase. The apparent
363 stiffness degrades as damage is produced and the deviatoric stress presents
364 a significant drop after having reached a peak. This strain level corresponds
365 to the predicted failure of the sample. It is worth noting that damage does
366 not depend on the material hydraulic behavior (equation 8). As a result, the
367 stress/strain curves obtained for both controlled capillary pressure tests are
368 strictly identical.

369 Figure 3 highlights the evolution of the volumetric fractions of voids (V_v),
370 natural pores (V_p) and cracks (V_c), as functions of the imposed axial defor-
371 mation. Before occurrence of any damage, the evolution of the volume of
372 voids (which is directly related to the porosity changes if the solid phase is
373 assumed incompressible) is solely due to changes of the volume of natural
374 pores. The volumetric behavior is contractant. As soon as cracks start to
375 appear, the decrease of the voids volume starts to slow down, and eventu-
376 ally the sample's volume starts to expand. The final rebound of the natural
377 pores' volume is due to the stress release after the stress peak.

378 One of the main strengths of the present model is to relate macroscopic
379 deformation to changes of the pore size distribution of the material. As a
380 consequence, the deformation of the natural porous network and the occur-
381 rence of cracking due to damage can clearly be observed in Figure 4, in terms
382 of PSD curve and cumulated porosity with pores radius. It shows the PSD
383 of the intact sample (continuous line - before loading) and of the damage

384 sample at the end of the deviatoric compression (dashed line). As expected,
385 the damaged material presents a bi-modal curve. Again, these PSD and
386 cumulated porosity curves are strictly identical whatever the imposed capil-
387 lary pressure because of the coupling assumptions. The values of the radii
388 corresponding to the two imposed pressures (through Laplace law) are also
389 shown. It can clearly be seen that the imposed capillary pressure of 300 kPa
390 corresponds to a radius (denoted r_{300} in the figure) belonging to the natu-
391 ral porous network. Inversely, for the other test, the capillary pressure of
392 100 kPa (denoted r_{100}) corresponds to a radius higher than the maximum
393 radius of natural pores, and is located within the range of radii of developing
394 cracks.

395 The knowledge of the evolution of the PSD enables the calculation of the
396 evolution of the retention properties and of the saturation state of the ma-
397 terial. In Figure 5, the water retention curves of the material are plotted at
398 three different stages of the test (initial (A), intermediate stage correspond-
399 ing to the maximum value of the degree of saturation (B) and final stage
400 (C)). It can be seen that at low degrees of saturation, the curve is shifted
401 upwards during the test. This means that for a given capillary pressure,
402 the volumetric fraction of voids saturated with the wetting phase tends to
403 increase. This corresponds to the compression of the smallest pores (natu-
404 ral network). Simultaneously, developing cracks form additional void space
405 made of large pores, that are easier to desaturate because cracks are charac-
406 terised by higher air entry radii. This explains why the part of the retention
407 curve defined for high degrees of saturation is ultimately shifted downwards
408 during the test. Figure 6 shows the evolution of the degree of saturation dur-

409 ing the tests performed at constant capillary pressures of 100 and 300 kPa.
410 It can be seen that for the test performed at the lowest pressure the material
411 starts at a saturated state (capillary pressure below the air entry value of the
412 rock) and becomes partially saturated when cracks open. A peak of degree
413 of saturation (at which the water retention curve denoted B in Figure 5 is
414 plotted) is observed for the second test. It corresponds to the lowest porosity
415 during the test.

416 The effects of deformation and damage of the material on the apparent
417 and intrinsic permeabilities can be caught through changes of the PSD curve.
418 This point is illustrated in Figure 7 which plots the evolutions of apparent,
419 intrinsic (top) and relative (bottom) permeabilities as a function of the ax-
420 ial deformation (left) and damage variable (right). Intrinsic permeability
421 (continuous lines of top sub-figures) decreases when the sample volume de-
422 creases and increases when damage becomes significant because the cracks
423 tend to facilitate fluid flow. Interestingly enough, the apparent permeability
424 (dash-dotted lines in top sub-figures) remains almost constant so that the
425 relative permeability present a trend which is totally the inverse of that of
426 the intrinsic permeability. In these tests, the total amount of water remains
427 located within the smallest natural pores and the contribution of these pores
428 to the water flow is not much affected by the deformation of the natural pores
429 network.

430 The permeability trends predicted by the model are now compared to
431 classical permeability models. Figure 8 shows the evolution of the intrin-
432 sic permeability (normalised by the value at the initial state) with porosity,
433 as predicted by the present model and by Kozeny-Carman model [59, 60].

434 The initial stage of the test, where porosity changes are dominated by com-
435 pressive deformation, follows reasonably well Kozeny-Carman equation. As
436 soon as damage occurs and porosity bounces back, the present simulations
437 show an increase of intrinsic permeability, corresponding to the growth of
438 the volumetric fraction of voids. Kozeny-Carman model cannot capture the
439 difference between the initial elastic pore compression and the subsequent
440 non-elastic pore creations related to the formation of cracks. As a result, the
441 crack-induced porosity increase is considered as an elastic expansion of the
442 volume of voids. The increase of permeability predicted by Kozeny-Carman
443 model follows the same path as the decrease of permeability due to elastic
444 compression (reversible path). It is worth noting that the trend predicted by
445 the proposed model is consistent with the experimental observations reported
446 in Figure 1 contrary to predictions based on Kozeny-Carman model.

447 Relative permeability evolution is compared to simple functions of the
448 degree of saturation (power laws). It can be observed that a satisfactory
449 fitting is observed (for both exponents 2 and 3 considered) when damage is
450 null or small and that the trends diverge when damage becomes significant.
451 This could be expected, since power laws have initially been proposed to
452 model retention properties in unimodal porous networks.

453 **5. Permeability and Retention Properties with Control of Water** 454 **Content**

455 Two compression tests followed by a conventional triaxial compression
456 are now simulated for fixed values of the water content, for the same rock
457 material (Table 1). These two tests correspond to water contents that are in

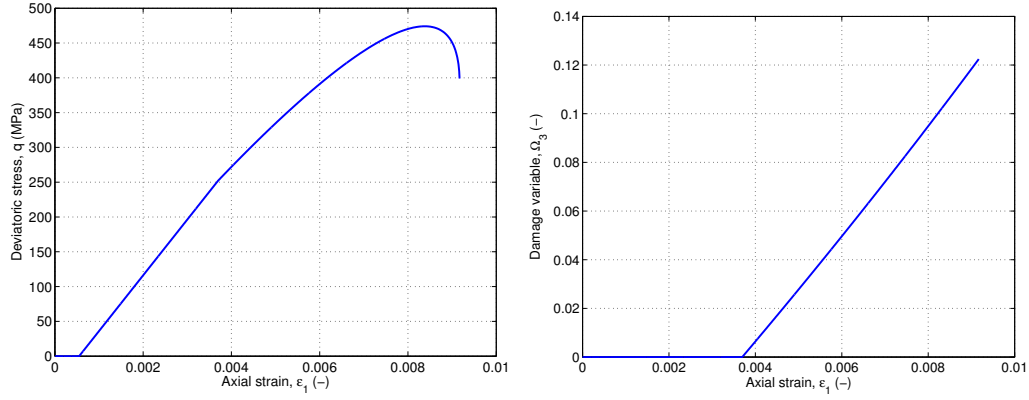


Figure 2: Stress/strain curve (left) and damage variable (right) during triaxial compression at constant capillary pressure $p_c = 100$ kPa.

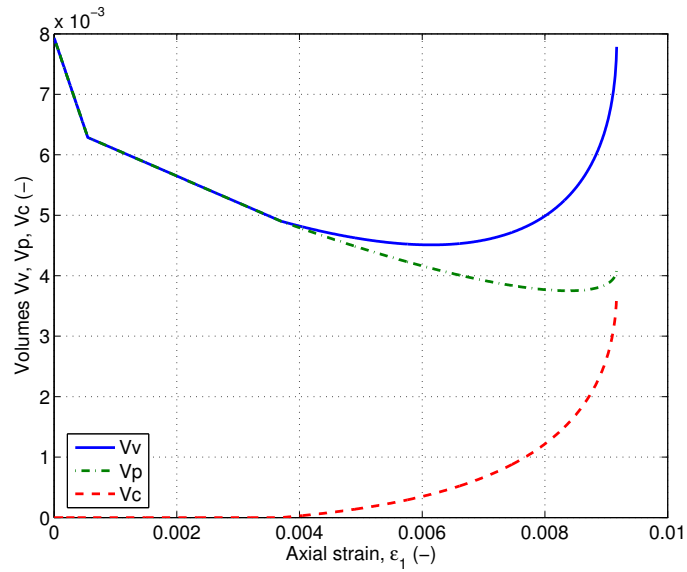


Figure 3: Evolution of volumes V_v , V_p and V_c during triaxial compression at constant capillary pressure $p_c = 100$ kPa.

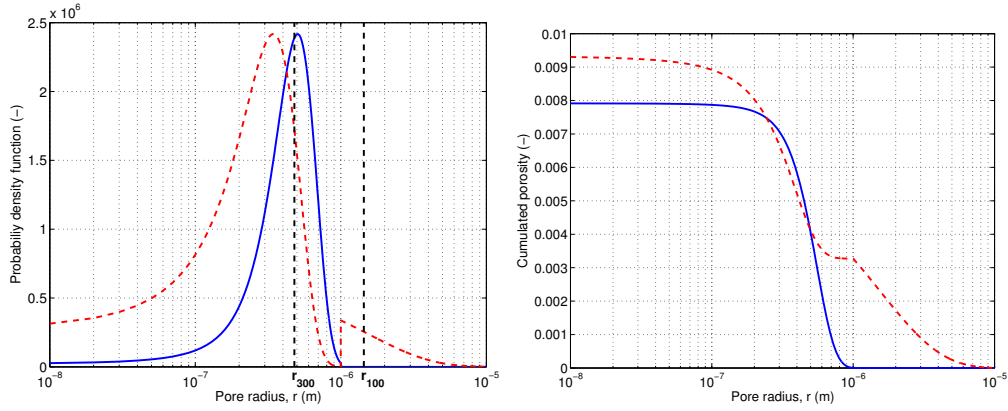


Figure 4: (Left) PSD curves (left) and cumulated porosity (right) vs pore radius of original (continuous line) and damaged (dashed-line) material during triaxial compression at constant capillary pressure. r_{100} (resp. r_{300}) denotes the value of the pore radius below which pores are saturated under a capillary pressure of $p_c = 100kPa$ (resp. $p_c = 300kPa$).

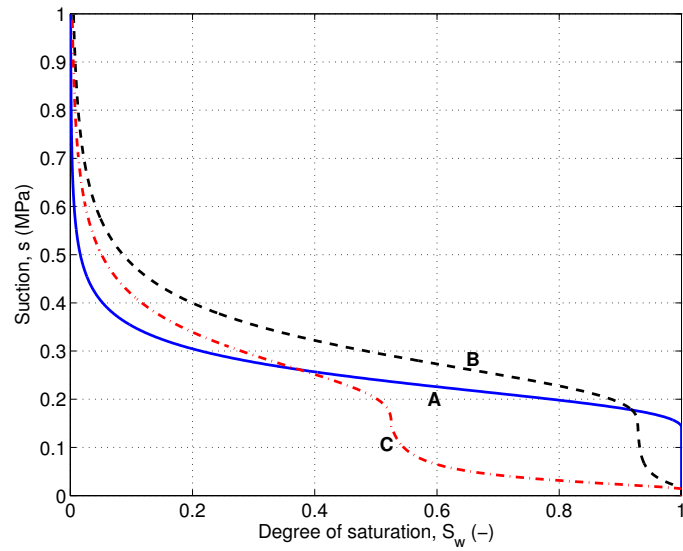


Figure 5: Water retention curves of the rock during the triaxial compression test under a constant capillary pressure of $p_c = 300$ kPa: initial state (A), damaged state with maximum degree of saturation (B), final state (C).

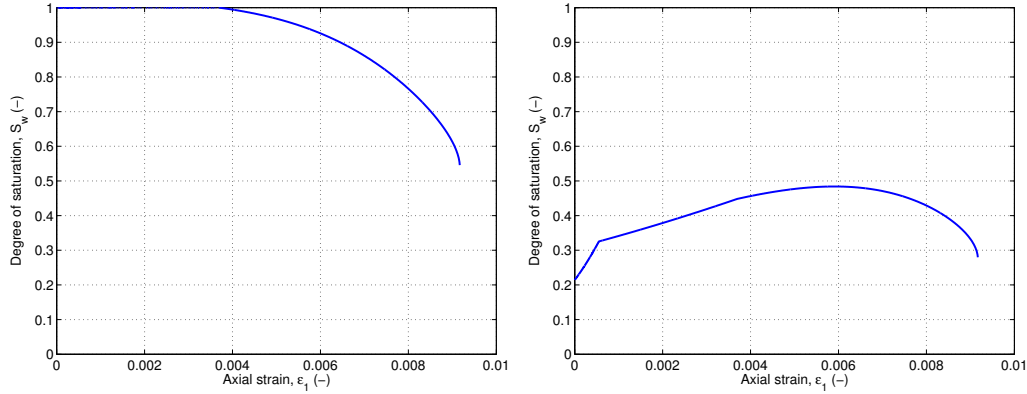


Figure 6: Evolution of degree of saturation during triaxial compression at constant capillary pressure: $p_c = 100$ kPa (left) and $p_c = 300$ kPa (right).

458 equilibrium at the initial state with capillary pressures (denoted $p_{c,0}$) of 300
 459 kPa and 500 kPa, respectively.

460 Figure 10 shows the evolution of the degree of saturation together with
 461 that of the capillary pressure (or suction) for the two compression tests. As in
 462 controlled suction tests and according to equation 29, the degree of saturation
 463 first increases (due to the decrease of the void ratio, dominated by elastic
 464 compression), and then decreases rapidly (due to the growth of the void
 465 space related to crack opening). In both cases, suction increases throughout
 466 the whole test. Initially, when the degree of saturation increases, the limit
 467 size of the saturated pores (r_{sat}) is located in the natural pores. Natural
 468 pore shrinkage due to elastic compression reduces r_{sat} , which corresponds to
 469 a capillary pressure increase according to equation 21. In the second stage,
 470 the degree of saturation decreases because of the creation of new void space
 471 in developing cracks.

472 Figure 11 shows the evolution of the relative permeability during the two

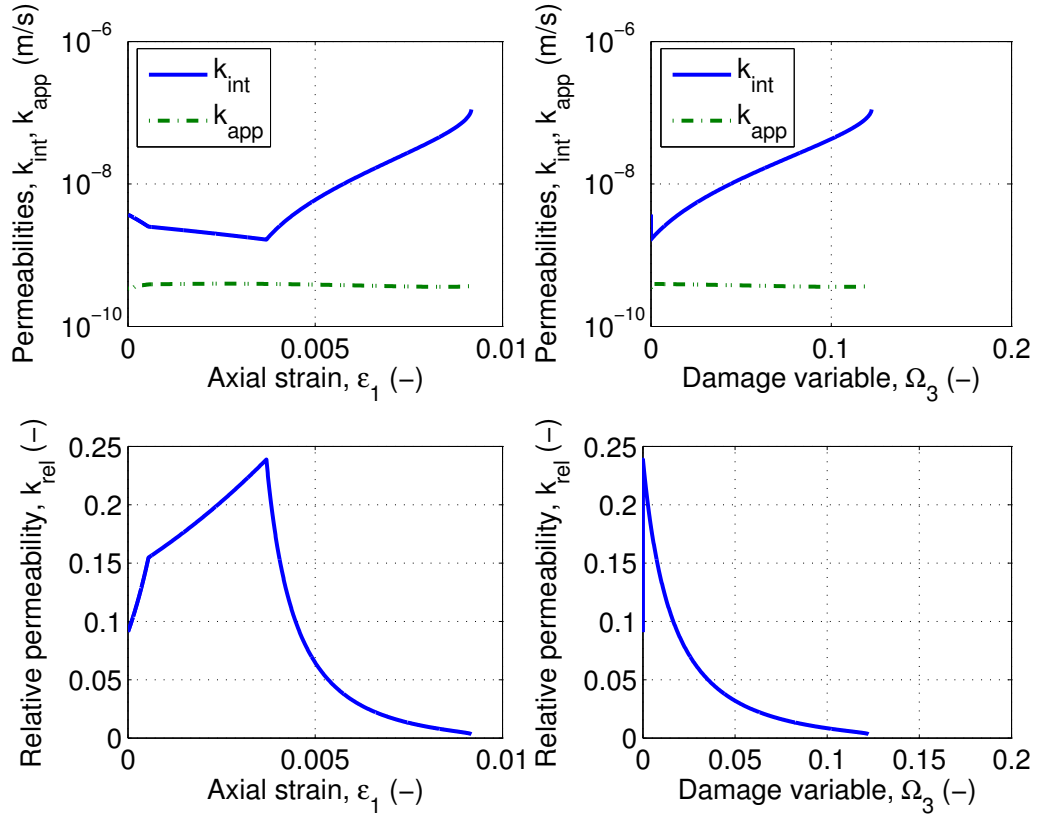


Figure 7: Evolution of total, intrinsic and relative permeabilities versus axial deformation (left) or damage variable (right) during triaxial compression at constant capillary pressure $p_c = 300$ kPa.

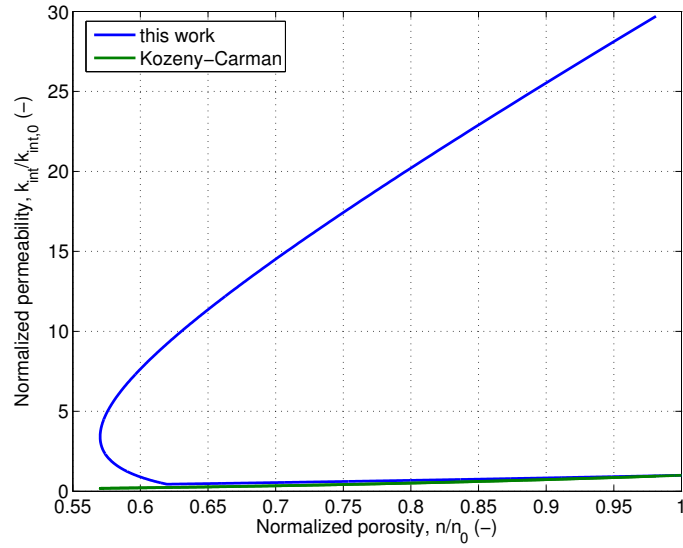


Figure 8: Evolution of the intrinsic permeability versus porosity during triaxial compression at constant capillary pressure $p_c = 100$ kPa.

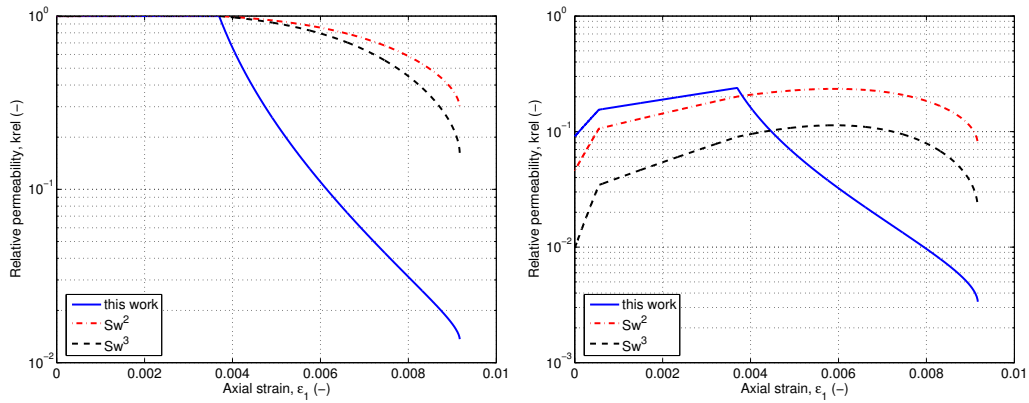


Figure 9: Evolution of the relative permeability during triaxial compression at constant capillary pressure: $p_c = 100$ kPa (left) and $p_c = 300$ kPa (right).

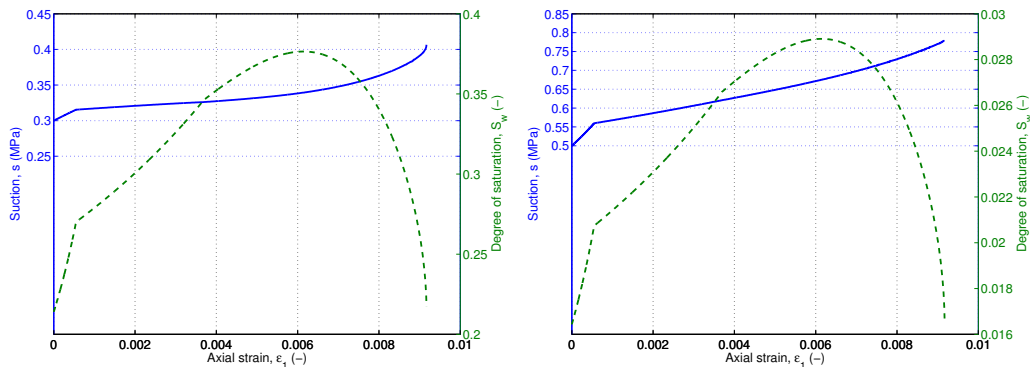


Figure 10: Evolution of suction and degree of saturation during triaxial compression at constant water content ($p_{c,0} = 300$ kPa (left) and $p_{c,0} = 500$ kPa (right)).

473 tests. A comparison with the trends given by the power laws used previously
 474 is performed. It can be observed that the predictions given by the present
 475 model, based on a microscopic approach, differ from the unimodal models of
 476 relative permeability. The differences are larger than in the previous suction-
 477 controlled tests, and are more important for high values of damage. This
 478 demonstrates the ability of the proposed model to capture microstructure
 479 changes. As explained before, suction variations are sensitive to the radius
 480 size distributions and to the limit size of saturated pores (r_{sat}). The tests
 481 performed at constant water content involve higher suctions than in the tests
 482 performed at constant capillary pressure, which emphasizes the difference
 483 between the current model predictions and classical power laws.

484 6. Conclusion

485 A permeability model is proposed for unsaturated cracked porous media.
 486 In all the tests simulated in the paper, the Representative Elementary Volume
 487 is assumed to be undamaged in the initial state. Initial porosity is associated

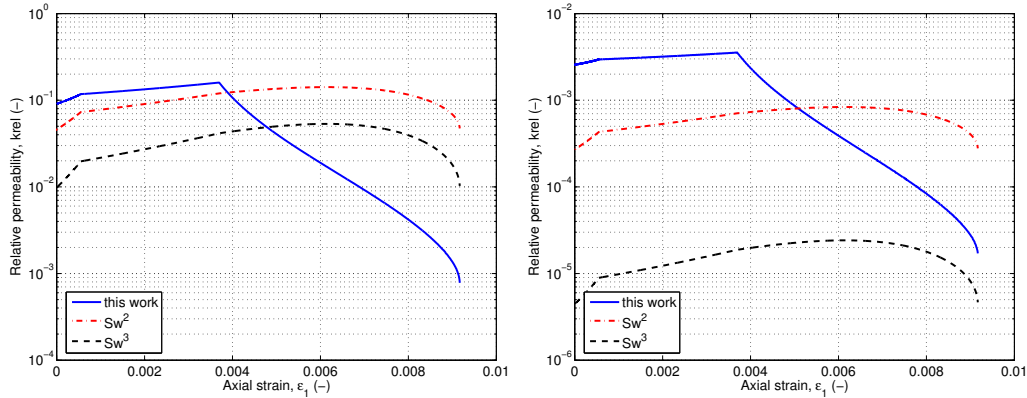


Figure 11: Evolution of relative permeability during triaxial compression at constant water content ($p_{c,0} = 300$ kPa (left) and $p_{c,0} = 500$ kPa, (right)).

488 to “natural pores” created before loading. Rock microstructure is charac-
 489 terized by the Size Distributions of natural pores and cracks. The volume
 490 occupied by the cracks is updated with damage-induced elastic and inelastic
 491 strains, whereas the volume occupied by natural pores is updated with purely
 492 elastic deformation. The conceptual model is general, and can be adapted to
 493 any damage constitutive model providing the evolution of damage-induced
 494 deformation. The intrinsic permeability of the damaged rock is updated with
 495 the volume fractions of natural pores and cracks, by using Hagen-Poiseuille
 496 flow equation and Darcy’s law. The void space occupied by water is com-
 497 puted by integrating the Pore Size Distributions (PSD) of natural pores and
 498 cracks up to the capillary pore radius (r_{sat}). The latter defines the size below
 499 which pores are saturated with water, and above which pores are saturated
 500 with air. Laplace equation is used to relate r_{sat} to the capillary pressure. The
 501 paper explains how to update PSD parameters with deformation and damage
 502 macroscopic variables, and then how to update the permeability and reten-

503 tion properties with the PSD parameters. The main original contributions of
504 the presented work are the prediction of the evolution of bimodal PSD curves
505 with crack propagation, and the relationship between deformation and dam-
506 age on the one hand and water retention curve and apparent permeability
507 on the other hand. Unconfined triaxial compression tests are simulated un-
508 der controlled capillary pressure and under controlled water content. The
509 proposed model captures well the intrinsic permeability decrease associated
510 to the elastic compression of the natural pores, followed by the permeability
511 jump due to crack opening. The PSD curves evolve with the deformation
512 and damage of the material. Obtained results catch the main features ob-
513 served in laboratory tests, such as: (1) the decrease of the characteristic size
514 of natural pores because of compression, and (2) the creation of much larger
515 pores corresponding to the damage-induced cracks. The model can also pre-
516 dict changes in the relative permeability during tests on partially saturated
517 materials. In particular, the model predicts that the apparent permeability
518 of the sample remains constant throughout a compression test performed at
519 constant capillary pressure, and that the suction keeps increasing in a com-
520 pression test performed at constant water content.

521 The proposed model requires a limited number of microscopic parameters,
522 which can easily be determined in the laboratory by Mercury Intrusion Tests
523 (for the PSD parameters) and by microscope observations (for the mini-
524 mum and maximum pore and crack sizes). The modeling framework can
525 be adapted to any rock constitutive model, including thermo-hydro-chemo-
526 mechanical couplings, and for problems related to damage or not. In par-
527 ticular, the effects of thermal expansion and chemical dissolution on rock

528 microstructure and porosity can be accounted for, as long as the appropriate
529 state equations and evolution functions are provided. The key issue con-
530 sists in splitting deformation in order to relate strain components to PSD
531 integrals. The approach is expected to facilitate multi-phase fluid flow pre-
532 dictions in cracked porous media. Potential applications may be found in
533 energy production, ore exploitation and waste management.

534 **References**

- 535 [1] D. Bourdet, *Well Test Analysis: the use of advanced interpretation mod-*
536 *els*, Elsevier, Amsterdam, The Netherlands, 2002.
- 537 [2] M. Honarpour, L. Koederitz, A. Harvey, *Relative permeability of*
538 *petroleum reservoirs*, CRC Press, Inc. Boca Raton, Florida, 1986.
- 539 [3] C. Zhao, B. Hobbs, A. Ord, *Convective and Advective Heat Transfer in*
540 *Geological Systems*, Springer, Berlin, 2008.
- 541 [4] C. Zhao, B. Hobbs, A. Ord, *Fundamentals of Computational Geoscience:*
542 *Numerical Methods and Algorithms*, Springer, Berlin, 2009.
- 543 [5] A. Gens, A. Garcia-Molina, S. Olivella, E. Alonso, F. Huertas, *Analy-*
544 *sis of a full scale in situ test simulating repository conditions*, *Interna-*
545 *tional Journal for Numerical and Analytical Methods in Geomechanics*
546 *22 (1998) 515–548*.
- 547 [6] C. Tsang, F. Bernier, C. Davies, *Geohydromechanical processes in the*
548 *excavation damaged zone in crystalline rock, rock salt, and indurated*

- 549 and plastic clays - in the context of radioactive waste disposal, Interna-
550 tional Journal of Rock Mechanics and Mining Sciences 42 (2005) 109–
551 125.
- 552 [7] H. Brandl, Energy foundations and other thermo-active ground struc-
553 tures, *Géotechnique* 56 (2006) 81–122.
- 554 [8] J. Lund, Characteristics, development and utilization of geothermal re-
555 sources, *Geo-Heat Center Bulletin* 28 (2) (2007) 1–9.
- 556 [9] I. Garcia-Bengoechea, C. Lowell, A. Altschaeffl, Pore distribution and
557 permeability of silty clays, *J. Geotech. Eng. Div.* 105 (1979) 839–856.
- 558 [10] M. VanGenuchten, A closed-form equation for predicting the hydraulic
559 conductivity of unsaturated soils, *Soil Science Society of America Jour-
560 nal* 44 (1980) 892–898.
- 561 [11] E. Romero, Characterisation and thermo-hydro-mechanical behavior of
562 unsaturated boom clay: an experimental study, Ph.D. thesis, Univeritat
563 Politecnica de Catalunya, Barcelona (1999).
- 564 [12] E. Rojas, G. Gallegos, J. Leal, A porous model based on porosimetry to
565 simulate retention curves, in: E. E. Alonso, A. Gens (Eds.), *Unsaturated
566 Soils - Proc. of the 5th Int. Conf. on Unsaturated Soils, Vol. 2*, CRC
567 Press, Barcelona, Spain, 2011, pp. 927–932.
- 568 [13] A. Russell, Water retention characteristics of soils with double porosity,
569 *European Journal of Soil Science* 61 (2010) 412–424.

- 570 [14] R. Salgueiro, S. Olivella, J. Suriol, Constitutive model developments for
571 compacted unsaturated fine grained soils based on porosimetry, in: E. E.
572 Alonso, A. Gens (Eds.), *Unsaturated Soils - Proc. of the 5th Int. Conf.*
573 *on Unsaturated Soils*, Vol. 2, CRC Press, Barcelona, Spain, 2011, pp.
574 951–956.
- 575 [15] H. Zhou, J. Shao, X. Feng, D. Hu, Coupling analysis between stress
576 induced anisotropic damage and permeability variation in brittle rocks,
577 *Key Engineering Materials* 340-341 (2007) 1133–1138.
- 578 [16] H. Gerke, M. VanGenuchten, A dual-porosity model for simulating the
579 preferential movement of water and solutes in structured porous media,
580 *Water Resources Research* 29 (1993) 305–319.
- 581 [17] J. Gwo, P. Jardine, G. Wilson, G. Yeh, A multiple-pore-region concept
582 to modeling mass transfer in subsurface media, *J. Hydrol.* 164 (1995)
583 217–237.
- 584 [18] T. Vogel, H. Gerke, R. Zhang, M. V. Genuchten, Modeling flow and
585 transport in a two-dimensional dual-permeability system with spatially
586 variable hydraulic properties, *J. Hydrol.* 238 (2000) 78–89.
- 587 [19] R. Zimmerman, T. Hagdu, G. Bodvarsson, A new lumped-parameter
588 model for flow in unsaturated dual-porosity media, *Adv. Water Resour.*
589 19 (1996) 317–327.
- 590 [20] W. Durner, Hydraulic conductivity estimation for soils with heteroge-
591 neous pore structure, *Water Resour. Res.* 30 (2) (1994) 211–223.

- 592 [21] J. Long, J. Remer, C. Wilson, P. Witherspoon, Porous media equivalents
593 for networks of discontinuous fractures, *Water Resources Research* 18 (3)
594 (1982) 645–658.
- 595 [22] R. Peters, E. Klavetter, A continuum model for water movement in an
596 unsaturated fractured rock mass, *Water Resources Research* 24 (1988)
597 416–430.
- 598 [23] K. Pruess, J. Wang, Y. Tsang, On thermohydrologic conditions near
599 high-level nuclear wastes emplaced in partially saturated fractured tuff.
600 2. effective continuum approximation., *Water Resour. Res.* 26 (1990)
601 1249–1261.
- 602 [24] H. Wong, C. Leo, J.-M. Pereira, P. Dubujet, Sedimentation-
603 consolidation of a double porosity material, *Computers and Geotechnics*
604 34 (2007) 532–538.
- 605 [25] K. Chan, S. Bodner, D. Munson, Permeability of wipp salt during dam-
606 age evolution and healing, *International Journal of Damage Mechanics*
607 10 (2001) 347–375.
- 608 [26] J. Shao, H. Zhou, K. Chau, Coupling between anisotropic damage and
609 permeability variation in brittle rocks, *International Journal for Numer-
610 ical and Analytical Methods in Geomechanics* 29 (2005) 12311247.
- 611 [27] J. Zhou, J. Shao, Xu, Coupled modeling of damage growth and perme-
612 ability variation in brittle rocks, *Mechanics Research Communications*
613 33 (2006) 450–459.

- 614 [28] K. Maleki, Modélisation numérique du couplage entre l'endommagement
615 et la perméabilité des roches - application à l'étude des ouvrages
616 de stockage souterrain, Ph.D. thesis, Ecole Nationale des Ponts et
617 Chaussées (2004).
- 618 [29] K. Maleki, A. Pouya, Numerical simulation of damage-permeability re-
619 lationship in brittle geomaterials, *Computers and Geotechnics* 37 (2004)
620 619–628.
- 621 [30] C. Arson, J.-M. Pereira, Influence of damage on pore size distribution
622 and permeability of rocks, *International Journal for Numerical and An-
623 alytical Methods in Geomechanics* (2012) DOI: 10.1002/nag.1123.
- 624 [31] R. Goodman, *Introduction to Rock Mechanics*, Second edition, Wiley,
625 1989.
- 626 [32] J. Jaeger, N. Cook, R. Zimmerman, *Fundamentals of rock Mechanics*,
627 Fourth edition, Blackwell Publishing, 2007.
- 628 [33] C. Alves, M. S. Braga, C. Hammecker, Water transfer and decay of
629 granitic stones in monuments, *C.R. Acad. Sci. Paris, serie IIa (Surface
630 Geosciences)* (1996) 397–402.
- 631 [34] J. Fortin, S. Stanchits, S. Vinciguerra, Y. Guéguen, Influence of thermal
632 and mechanical cracks on permeability and elastic wave velocities in a
633 basalt from mt. etna volcano subjected to elevated pressure, *Tectono-
634 physics* 503 (2011) 60–74.
- 635 [35] A. Byrnes, Reservoir characteristics of low-permeability sandstones in
636 the rocky mountains, *The Mountain Geologist* 34 (1997) 39–51.

- 637 [36] Y. Ghorbani, M. Becker, J. Petersen, S. Morar, A. Mainza, J.-P.
638 Franzidis, Use of x-ray computed tomography to investigate crack dis-
639 tribution and mineral dissemination in sphalerite ore particles, *Minerals*
640 *Engineering* 24 (2011) 1249–1257.
- 641 [37] F. Renard, D. Bernard, J. Desrues, A. Ougier-Simonin, 3d imaging of
642 fracture propagation using synchrotron x-ray microtomography, *Earth*
643 *and Planetary Science Letters* 286 (2009) 285291.
- 644 [38] S. Zabler, A. Rack, I. Manke, K. Thermann, J. Tiedemann, N. Harthill,
645 H. Riesemeier, High-resolution tomography of cracks, voids and micro-
646 structure in greywacke and limestone, *Journal of Structural Geology* 30
647 (2008) 876887.
- 648 [39] L. Dormieux, D. Kondo, F. Ulm, *Microporomechanics*, Wiley & Sons,
649 2006.
- 650 [40] P. A. Lock, X. D. Jing, R. W. Zimmerman, E. M. Schlueter, Predicting
651 the permeability of sandstone from image analysis of pore structure, *J.*
652 *Appl. Phys.* 92 (2002) 6311–6319.
- 653 [41] M. Kachanov, Effective elastic properties of cracked solids: critical re-
654 view of som basic concepts, *Appl. Mech. Rev.* 45 (8) (1992) 304–335.
- 655 [42] M. Ortiz, A constitutive theory for the inelastic behaviour of concrete,
656 *Mech. Mater.* 4 (1985) 67–93.
- 657 [43] R. AbuAlRub, G. Voyiadjis, On the coupling of anisotropic damage and
658 plasticity models for ductile materials, *Int. J. Solids A/ Struct.* 40 (2003)
659 2611–2643.

- 660 [44] A. Chiarelli, J. Shao, Modélisation élastoplastique couplée à
661 l'endommagement anisotrope induit pour les argilites, *Revue Française*
662 *de Génie Civil* 6 (1) (2002) 115–130.
- 663 [45] F. Homand-Etienne, D. Hoxha, J. Shao, A continuum damage consti-
664 tutive law for brittle rocks, *Computers and Geotechnics* 22 (2) (1998)
665 135–151.
- 666 [46] G. Swoboda, Q. Yang, An energy-based damage model of geomaterials
667 1. formulation and numerical results, *Int. J. Solids and Struct.* 36 (1999a)
668 1719–1734.
- 669 [47] J. Cordebois, F. Sidoroff, Endommagement anisotrope en élasticité et
670 plasticité, *Journal de Mécanique théorique et appliquée* (special issue)
671 (1982) 45–60.
- 672 [48] J. Chaboche, Development of continuum damage mechanics for elastic
673 solids sustaining anisotropic and unilateral damage, *International Jour-*
674 *nal of Damage Mechanics* 2 (1993) 311–329.
- 675 [49] D. Ronen, H. Scher, M. Blunt, On the structure and flow processes in
676 the capillary fringe of phreatic aquifers, *Transport in Porous Media* 28
677 (1997) 159–180.
- 678 [50] D. Ronen, H. Scher, M. Blunt, Field observations of a capillary fringe
679 before and after a rainy season, *Journal of Contaminant Hydrology* 44
680 (2000) 103–118.
- 681 [51] M. Blunt, Flow in porous media - pore-network models and multiphase
682 flow, *Current Opinion in Colloid & Interface Science* 6 (2001) 197–207.

- 683 [52] P. Delage, Y.-J. Cui, L'eau dans les sols non saturés, Techniques de
684 l'Ingénieur (C301) (2000) 1–20.
- 685 [53] R. Craig, Craig's Soil Mechanics, Seventh Edition, Spon Press, 2004,
686 Ch. 1, pp. 1–29.
- 687 [54] O. Coussy, Mechanics and Physics of Porous Solids, Wiley & Sons, 2010.
- 688 [55] T. Lacy, D. MacDowel, R. Talreja, Gradient concepts for evolution of
689 damage, Mechanics of Materials 31 (1999) 831–860.
- 690 [56] F. Homand, A. Chiarelli, D. Hoxha, Caractéristiques physiques et
691 mécaniques du granite de la vienne et de l'argilite de l'est, Revue
692 Française de Génie Civil 6 (1) (2002) 11–20.
- 693 [57] C. Arson, B. Gatmiri, Numerical study of a thermo-hydro-mechanical
694 damage model for unsaturated porous media, Annals of Solid and Struc-
695 tural Mechanics 1 (2010) 59–78.
- 696 [58] D. Halm, A. Dragon, Modélisation de l'endommagement par
697 mésofissuration du granite, Revue Française de Génie Civil 17 (2002)
698 21–33.
- 699 [59] J. Kozeny, Ueber turbulentes fließen bei glatten waenden., Ztschr.
700 angew. Math. und Mech. 5 (1925) 244–250.
- 701 [60] P. Carman, Fluid flow through granular beds, Transactions - Institution
702 of Chemical Engineers 15 (1937) 150–166.